Source and basin effects on rotational ground motions: comparison with translations

Haijiang Wang[1], Heiner Igel[1], František Gallovič[2], Alain Cochard[3]

[1]Department of Earth and Environmental Studies, Geophysics Section, Ludwig-Maximilians-University, München, Germany

[2]Department of Geophysics, Faculty of Mathematics and Physics, Charles University, Prague, Czech Republic

[3]Ecole et Observatoire des Sciences de la Terre, 5 rue René Descartes, 67084 Strasbourg Cedex, France

Corresponding Author:

Heiner Igel

Geophysics Section, Department of Earth and Environmental Sciences

LMU Munich,

Theresienstr. 41,

80333 Munich, GERMANY.

Room: 440

Phone: +49 (89) 2180-4204

Fax: +49 (89) 2180-4205

Email: heiner.igel@geophysik.uni-muenchen.de

ABSTRACT

The recent availability of accurate observations of rotational ground motions has re-opened interest in understanding near-fault characteristics of such motions in the context of strong ground motion and earthquake engineering. In order to investigate source and structure-dependent variations of rotational motions, we simulate several M7 earthquakes with varying source scenarios on the Newport-Inglewood (NI) fault embedded in the 3D Los Angeles basin using a finite difference method. We use a pre-calculated data base with several hundred numerical Green's functions for a discretized model of the NI fault that allows arbitrary finite-fault scenarios to be synthesized by superposition. We investigate source and basin effects on the rotational part of ground motion (namely maximum peak ground rotation rates and their variations) and compare them with the corresponding values of translational motion. Our main conclusions are: (1) the pure-strike slip source mechanism leads to larger rotation rates around the vertical axis than around the horizontal ones; (2) variation of hypocenter introduces more scatter on ground rotation rate than variations of slip history; (3) even relatively close to the fault there is considerable waveform similarity between the horizontal accelerations and the vertical rotation rates in the considered frequency range; (4) the co-processing of translations and rotations might reveal information on local velocity structure as indicated by plane wave theory; (5) the attenuation of accelerations (horizontal components) and rotation rate (vertical component) with distance from the fault are very similar, suggesting that similar expressions (as a function of distance) as for the peak accelerations can be adopted for the peak rotation rates when determining their attenuation relations.

Introduction

In conventional earthquake engineering, seismic loads on structures are formulated only in terms of the three translational ground motion components. Nevertheless, each site on the surface is subjected to six kinds of motions three translations along x-, y- and z-axes as well as three rotations about these axes (plus six components of strain in a deformable body). While the building response to translational motions has been thoroughly investigated, the study of building response to rotational motions is a relatively new field. The engineering importance of rotational components of seismic strong ground motion was noted during the late sixties and early seventies of the last century (e.g., Newmark and Hall, 1969; Newmark and Rosenblueth, 1971). There are many reports about rotations of tombstones and stone lanterns during large earthquakes (e.g., Yamaguchi and Odaka, 1974). Zembaty (2006) also pointed out that the rotation effects become especially important in the case of high buildings. Different studies have shown that rotational excitations around horizontal axes can be significant (e.g., Gupta and Trifunac, 1987, 1988, 1989, 1990, 1991). For example, rotational excitations around horizontal axes become important for tall structures supported by soft soil while excitations around the vertical axis can dominate the response of long and stiff structures supported by soft soils (Zembaty and Boffi, 1994). Such buildings are very sensitive to angular momentum carried by rotational waves.

Recent theoretical studies (e.g., Teisseyre, 2004; Boratynski and Teisseyre, 2004) and observational results (e.g., Nigbor, 1994; Spudich *et al*., 1995; McLeod *et al*., 1998; Spillman *et al*., 1998; Takeo, 1998) considered rotational motions excited by a distant seismic source. A first contribution was a simulation study of rotational effects by Bouchon and Aki (1982), who simulated rotational ground motions near earthquake

faults buried in layered media for strike-slip and dip-slip fault models, and obtained a maximum rotational velocity of 1.5×10^{-3} rad/s produced by a buried 30 km long strike-slip fault with slip of 1 m (seismic moment of 8×10^{18} Nm). Such small rotational motions are difficult to measure. Deployment of strong motion accelerographs in many seismic areas of the world during the past decades has produced data on translational components of motion during many strong earthquakes. This data describes strong motion in three orthogonal directions (two horizontal and one vertical), but because the spacing of the recording sites is much larger than the wavelengths of the recorded motions, little is known today about the accompanying differential and rotational motions in most areas of the world except some rare studies (e.g., Spudich *et al.*, 1995; Huang, 2003, Spudich and Fletcher, 2008).

In recent decades ring laser technology succeeded in detecting weak rotational motions radiated by earthquakes (McLeod *et al.*, 1998; Pancha *et al.*, 2000; Cochard *et al.*, 2006; Igel *et al.*, 2005, 2007). At teleseismic distances the seismic wave field can be well approximated by plane waves. Under this assumption, a direct comparison between rotation rate around a vertical axis and transverse acceleration (recorded by a standard seismograph) is possible – translations and rotations are in phase and their amplitudes are scaled by twice the horizontal phase velocity. Igel *et al.* (2005) studied the similarity between the collocated translations and rotations recorded by the ring laser. Their observations showed over a very broad frequency range (1–150 sec) that the waveforms have the expected similarity, and the amplitude ratios allow an accurate estimate of horizontal phase velocities (see also Igel *et al.*, 2005, 2007; Cochard *et al.*, 2006). However, in the near source region, the fundamental assumption of the above mentioned study – plane wave propagation – might be violated.

Translational and rotational components of strong motion radiated from an

earthquake source are modified along the propagation path through interference, focusing, scattering, and diffraction phenomena. In this paper, we investigate how ground rotation rates vary for a given slip history and varying hypocenter location, as well as fixed hypocenter location and varying slip history, by means of numerical modeling considering realistic quasi-dynamic source and 3D velocity models. The results are compared with the corresponding effects on translations.

Numerical Green's Functions

In the following we describe the basic concept of the "numerical Green's functions" (NGF) approach and verify it against high-resolution ("continuous") finite-fault solutions. A target fault plane is divided into equal-sized rectangular subfaults and for each of these subfaults, the corresponding ground response, denoted as NGF, is calculated using a double-couple source mechanism (pure strike-slip) with an impulse-like slip velocity function. Then, a finite-source scenario can be synthesized by superposition of these NGF's convolved with appropriate slip functions. More detailed information about this method can be found in Wang (2007) and Wang *et al.* (2008, equation (1) to (4)). The forward calculations can be carried out using any numerical solution to the 3D wave propagation problem. Here we employ a high-order (4-th order in space, 2nd order in time) staggered-grid finite-difference approach (e.g., Igel *et al*., 1995; Graves, 1996, Ewald et al., 2006) with efficient absorbing boundaries based on the concept of perfectly matched layers (e.g., Collino and Tsogka, 2001; Marcinkovich and Olsen, 2003) and averaging of elastic moduli and densities to avoid diffraction effects (Moczo et al., 2002). The components of the vector of rotation is extracted by calculating half the curl of the wavefield at the surface.

We apply the NGF method to the Newport Inglewood (NI) fault system located in the Los Angeles (LA) basin (Fig. 1). An area of 96×87×25.5 km, in the two horizontal and vertical directions, is selected as the study area, being rotated in order to have the x-axis parallel to the NI fault. The velocity model is based on the elastic part of the SCEC 3D velocity model for the LA basin (Version 3, Kohler *et al.*, 2003). The depth of a shear wave velocity isosurface, 2.0 km/s, is shown in Fig. 2. To reduce the computational effort and the size of the data base, we truncate the seismic velocities at 1.4 km/s, which gives a maximum frequency resolution of 0.56 Hz with our grid spacing of 0.3 km (Wang et al., 2008).

The NI fault is chosen for several reasons: it hosted the M6.4 Long Beach earthquake in 1933 (Hauksson and Gross, 1991), causing serious damage, and it is still considered the most probable source for a damaging M7 earthquake in the LA area (USGS). The near-vertical plane can be simply approximated by a vertical plane in the numerical calculation, and the predominant right-lateral slip can be approximated with a pure strike-slip mechanism (Grant and Shearer, 2004). The possible small rupture geometry variations of such a mature fault are assumed to play only a minor role (Gallovič *et al*., 2008).

First, as done for the velocity part of ground motion by Wang *et al*. (2008), we determine the fault discretization that provides sufficiently accurate synthetics. The computational setup and source parameters are given in Table 1. We characterize the hypothetical M7 earthquake by fault length *L* and width *W* equal to 36 km and 18 km, respectively. The “continuous” solution has 120x60 subfaults of side 0.3 km, which corresponds to the grid minimum distance in the FD mesh. The quasi-dynamic rupture process is calculated according to the method published in Guatteri *et al*. (2004). In this model the rupture evolution (including slip velocities) is determined from a given

realization of random slip distribution described by a 2D Gaussian auto-correlation function. In our case we use an isotropic correlation length of 5 km for both the strike and dip directions. An example of a realization of such a final slip distribution is shown in the inlet of Fig. 1.

An M7 finite fault earthquake scenario is first simulated with all the 120x60 subfaults (treated as the “continuous” solution). The ground rotation rates are then synthesized from a coarser fault discretization (namely 5x5 and 6x6 FD grid points) and compared to the “continuous” solution. Fig. 3 shows the results of the verification. The *z*-component of rotation rate has much larger amplitude (and error) than the other two components (not shown) because of the pure-strike slip source mechanism, and thus is used to illustrate the results. The peak ground rotation rates (PGRRs) covering frequencies up to 0.5 Hz for different source discretizations are compared over the entire study area. Fig. 3a shows spatial (map) distribution of the relative PGRR difference, i.e. the difference between PGRRs for a discretized solution and the “continuous” one divided by the PGRR of the “continuous” solution. The largest relative difference is only 18% at the point denoted as P1 in that figure. In fact, the waveforms for different discretizations are almost identical as can also be seen from the waveform comparison (Fig. 3b) for point P1, where the largest relative PGRR difference is observed. Additionally, Fig. 3c compares waveforms for different discretizations along he EE’ profile (see Fig. 3a). The lowest correlation coefficient value is 0.991. In conclusion, we further use solutions with 1.5 km subfault side-length as they are accurate enough for M7 scenarios earthquakes under study.

Earthquake Scenario Simulations

The pre-calculated NGF data base allows us - within the limits of the method (e.g., reliable frequency range) - to synthesize ground motions from arbitrary strike-slip histories on the NI fault for the complete study area. How variations of the source parameters (namely hypocenter location and slip distributions) influence the shaking for a *scenario* earthquake is known to be of considerable relevance for the estimation of seismic hazard. This is the question we will focus on in this study for the potentional case of an M7 eartqhuake on the NI fault. In other words, the aim is to investigate the composite effect of the 3D structure and the source complexity on the ground rotation rates, and to provide a possible range of the ground rotation rates that might be generated by an M7 earthquake on the Newport Inglewood fault. The results are shown and analyzed in the following sections. Let us emphasize that we use quasi-dynamic slip histories, which are generated following the approach by Guatteri *et al.* (2004).

Effect due to Hypocenter Location

In this section we investigate how variations of the hypocenter location for a given final slip distribution influence the ground rotation rate. A 4x6 grid of possible hypocenters in the seismogenic zone (5 - 15 km depth), as indicated in the inlet of Fig. 1, is considered. For each of these hypocenters the ground rotation rates are synthesized and analyzed. From the NGF database, six-component seismograms are synthesized for the entire surface grid of receivers. Only the peak ground rotation rates are discussed.

In Fig. 4 we show maps of ground rotation rate due to varying hypocenter location in terms of maximum ground rotation rates and their variations. The maximum values

describe how fast a station could rotate during *scenario* M7 earthquakes. In this study one of our aims is to quantify the *variations* of ground rotation characteristics due to source characteristics. To this end, two ratios are considered: R_{SD} – standard deviation relative to mean value, and R_{max} – maximum value divided by mean value. R_{max} quantifies the expected variations in specific regions.

At first glance, all the maps in Fig. 4 exhibit complex patterns. The largest rotation rate of the entire study area for the vertical component is 8 times larger than those of the x-component and 5 times larger than those of the y-component. This phenomenon can be attributed to the source mechanism (pure strike slip). The maximum rotation rate over the entire study area is observed close to the fault trace (inside region A), but at varying places for different components. In region A (surrounding the fault trace), for the x-component, the maximum PGRR distribution is quite symmetrical about the middle of the fault trace in the x direction (Fig. 4 top left). This symmetry is observed to a lesser extent for the other two components (Fig. 4 middle left and bottom left). For the y- and z-components, larger values can be observed even further from the fault (in the basin – region B). This suggests that in our model the fault parallel component of rotation rate, i.e., the x-component, is more affected by the source and less affected by the 3D structure than the other two components.

The ground motion variation due to varying hypocenters is illustrated by showing the spatial distribution of the R_{SD} ratio (Fig. 4 middle column). We focus on the two regions B and C, where substantial basin depth variations are located, to illustrate the 3D effect on rotations. For the x-component, there is no noticeable high R_{SD} (Fig. 4 top middle) inside these two regions. However for the y-component (Fig. 4 middle middle) and the z-component (Fig. 4 bottom middle), a large R_{SD} is observed when compared to the neighbouring areas. The largest R_{SD} of the whole study area, 75% for the y-component

and 72% for the z-component, are all located inside region C. Right on the fault trace, the R_{SD} ratio for the x-component (Fig. 4 top middle) is similar to that in the neighbouring regions. On the contrary, for the other two components (Fig. 4 middle middle and bottom middle) the values above and close to the fault are smaller than those further from the fault. For all three components, but especially for the z-component, large R_{SD} values are found in the regions off both tips of the fault trace.

The distributions of the R_{max} ratio are shown in Fig. 4 (right column). For the y- and z-components (Fig. 4 middle right and bottom right), large values are observed in regions B (small basin) and C (i.e., same as for R_{SD}). Moreover, the largest R_{max} over the entire study area lays at the same positions (P1 for the y-component and P2 for the z-component) as for the R_{SD} case. Small values are observed near the fault plane (region A) when compared to the neighbouring areas. For the x-component, the largest R_{max} is at station P3 whereas the largest R_{SD} is at station P4. At some places, the rotation rates can be 2 to 3 times larger than the mean rotation rates, and this for all components.

Effect due to Slip History

Variation of strong ground motion observed in the near-source is associated with several phenomena like directivity, near-source effect, and static offsets, etc., which are strongly affected not only by the hypocenter position but also by the geometrical and dynamic characteristics of the slip history. Therefore, for a fixed hypoenter, we generate 20 random slip distributions, each corresponding to a M7 earthquake, with the quasi-dynamic approach of Guatteri *et al.* (2004).

The results are shown in Fig. 5, in the same was as in Fig. 4. As in the previous case, the mapped quantities exhibit complex behaviour. The largest rotation rate of the entire study area for the vertical component is 4.5 times larger than those of the x-

component and 6 times larger than those of the y-component. These largest rotation rates are located either right above (x- and z-component, Fig. 5 top left and bottom left) or very close to the fault trace (y-component, Fig. 5 middle left). For the y-component, the largest rotation rate happens around the epicenter, while those for the other two components are located further from the epicenter (on the fault trace, close to the far right end of the fault trace). Further from the fault trace, e.g., around point D, there are still large values for the y-component (Fig. 5 middle left) which are comparable to those on the fault trace. On the other hand, for the x- and z-components the rotation rates around point D are much smaller than those on the fault trace.

The spatial distributions of R_{SD} for all 20 simulations are shown in Fig. 5, middle column. The largest R_{SD} of the entire study area are similar for all components (42% for the x-component, 50% for the y-component and 45% for the vertical component), but not located at the same places. For the x-component, R_{SD} is very large inside region F which is around the epicenter. For the other two components, the high ratios are restricted inside region A (banded region perpendicular to the fault trace). At point G (small basin edge), higher ratios are found for the y- and z-components, but not for the x-component when compared to those areas around the fault trace (region F). Above the fault, varying slip histories introduce more variations on the fault parallel component of rotation rate than on the other two components.

The spatial distributions of the R_{max} ratio are shown in Fig. 5, right column. These distributions are quite similar to those for R_{SD}: the largest values of the entire study area are observed in the same areas. Around the epicenter, large R_{max} values are observed for the x-component but not for the other two components, for which large values of R_{max} are mostly restricted to region A (banded region perpendicular to the fault trace). High R_{max} values are observed at point G (basin edge) for the z-component. The spatial

distributions of R_{max} tend to be more localized than those of R_{SD}.

Finally, comparing the results shown in Fig. 4 and Fig. 5, in terms of R_{SD} and R_{max} (middle and right columns) we can observe that varying the hypocenter has a stronger effect than keeping the hypocenter fixed and varying slip histories. The specific spatial pattern of Fig. 5 (regions A, G), might be influenced by the "fixed" directivity effect due to the fixed source location.

Comparison with Translations

For a horizontally polarized plane wave, the horizontal (transverse) acceleration and the vertical rotation rate have identical waveforms; they are scaled by a factor related to the phase velocity (e.g., Igel *et al.,* 2005; 2007). In the following, we compare synthetic vertical rotation rates and horizontal accelerations simulated for the M7 hypothetical earthquake on the NI fault. This allows us to verify whether wavefronts are (near-) planar and whether it is appropriate to relate peak amplitudes of translations and rotations and whether it is feasible to estimate (at least roughly or to the first order) local phase velocities.

Comparison of waveforms

We study waveforms computed at three profiles, OR, PS and QT (see Fig. 5, bottom right) assuming a fixed hypocenter on the right of fault (that denoted H in Fig. 1 inlet). The rotation rate seismograms along these profiles are plotted in Fig. 6 for the two horizontal accelerations and the vertical rotation rate. Along profile OR, both the acceleration and the rotation rate attenuate faster with increasing y than along the other two profiles. In the range of $y < 26$ km, the major parts of the waveforms for the y-component of acceleration and the rotation rate are similar, but not for the x-component

of acceleration. Along profile PS, waveforms for the x-component of acceleration and rotation rate are almost identical when y > 22 km while the y-component of acceleration is different. For stations y < 16 km, the waveforms for the x-component of acceleration and for the vertical rotation rate are similar, but in an anti-correlated way. Along profile QT, for stations y > 25 km, the accelerations (x-component) and the rotation rates are almost identical in waveform while this similarity is not observed for the y-component of acceleration.

To quantify the waveform similarity for the entire study area, the zero-lag correlation coefficient (ZLCC) between two seismograms (one of the two horizontal accelerations and the vertical rotation rate) at a station is calculated and the results are shown in Fig. 7 for the same scenario as above. The higher the ZLCC, the more similar the waveforms. ZLCC equal to 1 means that the two seismograms are identical (regardless the absolute amplitude difference). For the x-component of acceleration (Fig. 7 left) the ZLCCs are larger than 0.75 for most of the area under study. The highest ZLCC is found in the y-direction from the epicenter. These regions of high ZLCC are expected from the source radiation pattern of strike slip sources and correlation of transverse acceleration with vertical rotation rate (assuming well-developed plane waves).

The fault perpendicular component of acceleration (Fig. 7 right) shows similar behaviour, only rotated by 90° around the hypocenter. In this way, best agreement is found in the strike direction off the fault. Again, this can be understood as a consequence of the radiation pattern and that in that direction the y-components are dominated by transverse type of motion. The waveform similarity seems to be slightly decreased to the left of the fault, possibly due to interaction with the basin.

Amplitude Ratio and Medium Parameter

Since in most of the study area, one of the horizontal component of acceleration is quite similar to the vertical rotation rates, it should be instructive to show the amplitude ratios between that component and the rotation rate, as has been done by Igel *et al*. (2005, 2007) for the transverse component of acceleration. Based on shear plane wave propagation, the amplitude ratio between the horizontal acceleration and the vertical rotation rate at a station is twice the phase velocity (Igel *et al*., 2005). The ratios should be smaller inside the basin than outside since the basin is characterized by smaller velocities. We denote mean value of the peak ground accelerations as M_{PGAx} and M_{PGAy} for the x and y components, respectively. The mean value of the peak vertical rotation rate is denoted as M_{PGRRz}.

Fig. 8 shows ratios M_{PGAx} / M_{PGRRz} and M_{PGAy} / M_{PGRRz} in map view (omitting the factor 2), together with the basin depth (iso-surface of the 2 km/s shear wave velocity), for the cases of varying hypocenter (left column) and varying slip history (right column). For the x-component of acceleration (Fig. 8 top) the ratios are small inside the basin. Outside of the basin, except for region A, the estimated ratio is higher. In region A the ratio is still low, which is not in agreement with the larger velocities therein. This is not surprising because the waveforms themselves are not so similar for the x component (see Fig. 7 left). In regions close to the left tip of the fault trace, when varying either hypocenter location or slip history (Fig. 8 top), the ratio is distinctly larger than 4000 m/s, being much larger than those in the neighbouring areas and not compatible with the velocity model. In such areas, however, the assumption of an incoming plane wave is violated.

For the y-component of acceleration (Fig. 8 middle row), in region B (being outside

the basin and thus characterized by large velocities), the ratio between the acceleration and the vertical rotation rate is less than 1700 m/s for the varying hypocenter case (Fig. 8 middle left). This suggests that there is no strong relation between the amplitude ratio and the basin structure, which is due to the position of the basin with respect to the fault where the waveforms are not similar, as shown in Fig. 7 (right) in terms of the correlation coefficient. In the strike direction, the predicted ratios are larger, corresponding to larger velocities outside the basin. For the varying slip history case (Fig. 8 middle right), the ratios in region A are higher (corresponding to higher velocities in that area), which is, however, perhaps only accidental, since in region C the ratios are again higher than what would correspond to the local velocities. On the other hand, off the fault in the strike direction, the ratios correspond to the velocity model as explained in the test presented in Fig. 7 (right).

A map of the average between the two ratios discussed above, $1/2(M_{PGAx} + M_{PGAy})/M_{PGRRz}$, is shown in Fig. 8 (bottom) for both varying hypocenter (left) and varying slip history (right). A strong relation between this average and the local velocity is observed almost over the entire study area [[coch: how can one judge?]] in these two cases. Large values of this parameter nicely delineate the basin structure. The only exceptions are the small regions around the tips of the fault trace where the plane wave assumption is clearly violated.

Decay with Distance

It is of practical importance to study how the peak rotation rates decay with distance. In particular, one can ask to what extent is the decay comparable to the decay known for peak translation motion (PGA, PGV, etc.), which is usually characterized by the attenuation relations.

In Fig. 9, we show the maximum amplitude of both the y-component of acceleration and the vertical rotation rate synthesized for the case of varying hypocenter location, and plot them against distance to the fault. At first glance, the shapes of the “point clouds” are very similar. Both the acceleration and the rotation rate saturate in for fault distances less than 10 km. It is also seen that the mean rotation rate decreases with fault distance similarly to acceleration for fault distances larger than 10 km. Local increase of largest values is observed for both the rotation rates and the accelerations within range A (between 25 and 53 km). It covers the small basin depicted as region B in Fig. 4, suggesting that the rotation rates are amplified in a way similar to acceleration by this small basin.

In conclusion, rotation rate linearly decreases with fault distance in log-log coordinates just as acceleration does. This suggests that when developing attenuation relationships for rotational motions, similar expressions (as a function of distance) as for the peak acceleration can be adopted.

Conclusions and Discussions

We investigated how variability of source model and 3D structure affect ground rotation rates. In the region surrounding the fault trace, the vertical component of rotation rates is systematically several times larger than the other two horizontal components, showing that the source mechanism (pure-strike slip) dominates the ground rotation rates in this region.

Variation in hypocenter location leads to large variations of the ground rotation rates. The fault perpendicular component of acceleration and the vertical rotation rates are

strongly affected by both the medium (basin structure) and the slip asperity location. However, there are no obvious effects of either the medium or the slip asperity location on the fault parallel component. That component is dominated by the directivity effect. The basin effect is also observed for the variations of the y and z components of the peak rotation rates, the largest variations being located at the basin edges. In the region close to the fault, where large rotation rates are observed, the variations are small. Hence, not only the hypocenter location but also the medium elastic properties control the rotation rate variations.

For the case of varying slip history, the directivity effect (if present) dominates the fault parallel component in terms of absolute values and relative variations. These variations are, however, smaller than those for the case of varying hypocenter location. The velocity medium effect is mainly pronounced on the fault-perpendicular component when considering the maximum value. The variations of the rotation rates are largest in the basin structure, especially for the y and z components.

Vertical rotation rates can be compared to horizontal accelerations as was done on the global scale by Igel *et al.* (2005, 2007). These authors theoretically derived, assuming plane wave incidence, the relation between the horizontal accelerations and the vertical rotation rates. The waveforms are identical, only scaled by twice the local phase velocity. In our study, we have found areas where the waveform of one component of the horizontal acceleration was very similar to the vertical rotation rate waveform. This is consistent with the shear wave radiation pattern of a double couple. The fault-parallel component of acceleration is similar to the vertical rotation rate in areas perpendicular to the fault strike, while the fault-normal component of acceleration is highly correlated to the vertical rotation rate in the strike direction of the fault. Therefore, waveform similarity is observed over the entire study area for at least one of the

acceleration horizontal component. When the average of these ratios is considered, a good agreement is obtained over the whole area under study. We have found good correlation with the velocity model except for a very small region surrounding the fault trace. This suggests a new tool for basin edge detection based on the co-processing of translational and rotational ground motion.

Finally, vertical rotation rate is found to decay with distance in a way very similar to acceleration. Therefore, similar expressions (as a function of distance) as peak acceleration can be adopted for rotational motions attenuation relationships.

Acknowledgements

This work was partially funded by the International Quality Network - Georisk (German Academic Exchange Service), and the Elite Graduate College THESIS (elite.geophysik.uni-muenchen.de). F.G has been supported by Grant Agency of the Czech Republic (205/08/P013) and MSM0021620800. We also acknowledge support from the European Human Resources Mobility Programme (Research Training Network SPICE, www.spice-rtn.org) and the provision of computational resources through the Leibniz Computing Centre Munich. We also thank KONWIHR for their support.

References

Boratynski, W. and R. Teisseyre (2004), Generalized continuum with defects and asymmetric stresses. *Acta Geophys Pol*, **52**, 185–195.

Bouchon, M. and K. Aki (1982), Strain, tilt, and rotation associated with strong ground motion in the vicinity of earthquake faults. *Bull. Seism. Soc. Am.*, **72**, 1717–1738.

Cochard, A., H. Igel, A. Flaws, B. Schuberth, J. Wassermann, and W. Suryanto (2006), Rotational motions in seismology, in: *Earthquake source asymmetry, structural media and rotation effects*, edited by Teisseyre *et al.*, Springer Verlag.

Collino, F., and C. Tsogka (2001), Application of the PML absorbing layer model to the linear elastodynamic problem in anisotropic heterogeneous media, *Geophysics*, **66**, 294-307.

Ewald, M., H. Igel, K. G. Hinzen, and F. Scherbaum (2006), Basin-related effects on ground motion for earthquake scenarios in the Lower Rhine Embayment, *Geophys. J. Int.*, **166**, 197-212.

Gallovič, F., M.Käser, J. Burjánek, and Ch. Papaiannou (2008), 3-D Modeling of Near-Fault Ground Motions of the 2004 Parkfield Earthquake with Non-Planar Rupture Models and Topography, *submitted to J. Geophys. Res*.

Grant, L. B., and P. M. Shearer (2004), Activity of the offshore Newport - Inglewood Rose Canyon fault zone, coastal Southern California, from relocated microseismicity, *Bull. Seism. Soc. Am.,* **94**, 747-752.

Graves, R. W. (1996), Simulating seismic wave propagation in 3D elastic media using staggered grid finite differences. *Bull. Seism. Soc. Am.*, **86**, 1091-1106.

Guatteri, M., P. M. Mai, and G. C. Beroza (2004), A pseudo-dynamic approximation to dynamic rupture models for strong ground motion prediction. *Bull. Seism. Soc. Am.,* **94**, 2051–2063.

Gupta, I. D. and M. D. Trifunac (1987), Statistical analysis of response spectra method in earthquake engineering. Dept Civil Eng, Univ Southern California, Los Angeles CA, report.

Gupta, I. D. and M. D. Trifunac (1988), A note on computing the contribution of rocking excitation to earthquake response of simple buildings. *Bull Indian Soc Earthq Tech*, **25:2**, 73–89.

Gupta, V. K. and M. D. Trifunac (1989), Investigation of building response to translational and rotational earthquake excitations. Dept Civil Eng, Univ Southern California, Los Angeles CA, Report.

Gupta, I. D. and M. D. Trifunac (1990), Probabilistic spectrum superposition for response analysis including the effects of soil-structure interaction. *J Probabilistic Eng Mech*, **5**, 9–18.

Gupta, V. K. and M. D. Trifunac (1991), Effects of ground rocking on dynamic response of multistoried buildings during earthquakes. *Struct Eng/Earthq Eng (JSCE),* **8:2**, 43–50.

Hauksson, E., and S. Gross (1991), Source parameters of the 1933 Long Beach earthquake, *Bull. Seism. Soc. Am.,* **81**, 81-98.

Huang, B. S. (2003), Ground rotational motions of the 1999 Chi-Chi, Taiwan earthquake as inferred from dense array observations. *Geophys. Res. Lett.*, **30**, 1307-1310.

Igel, H., U. Schreiber, A. Flaws, B. Schuberth, A. Velikoseltsev, and A. Cochard (2005), Rotational motions induced by the M8.1 Tokachi-oki earthquake, September 25, 2003. *Geophys. Res. Lett.,* **32**.

Igel, H., A. Cochard, J. Wassermann, A. Flaws, U. Schreiber, A. Velikoseltsev, and N. P. Dinh (2007), Broad-band observations of earthquake-induced rotational ground motions, *Geophys. J. Int.*, **168**, 182-197.

Igel, H., P. Mora and B. Riollet (1995), Anisotropic wave propagation through finite-difference grids, *Geophysics*, **60**, 1203-1216.

Kohler, M., H. Magistrale, and R. Clayton (2003), Mantle heterogeneities and the SCEC three-dimensional seismic velocity model version 3, *Bull. Seism. Soc. Am.,* **93**, 757-774.

Marcinkovich, C., and K. B. Olsen (2003), On the implementation of Perfectly Matched Layers in a 3D fourth-order velocity-stress finite-difference scheme, *J. Geophys . Res.*, **108**, 2276-2293.

McLeod, D. P., G. E. Stedman, T. H. Webb, and U. Schreiber (1998), Comparison of standard and ring laser rotational seismograms. *Bull. Seism. Soc. Am.,* **88**, 1495-1503.

Moczo, P., Kristek, J., Vavrycuk, V., Archuleta, R.J., Halada, L. (2002), 3D heterogeneous staggered-grid finite-difference modeling of seismic motion with volume harmonic and arithmetic averaging of elastic moduli and densities, Bull. Seism. Soc. Am., 92(8), 3042-3066.

Newmark, N. M. and H. J. Hall (1969), Seismic design criteria for nuclear reactor facilities. Proc. Fourth World conf Earthq Engrg. Santiago, Chile.

Newmark, N. M. and E. Rosenblueth (1971), Fundamentals of earthquake engineering Prentice-Hall, Englewood Cliffs.

Nigbor, R. L. (1994), Six-degree-of-freedom ground-motion measurement. *Bull. Seism. Soc. Am.*, **84**, 1665–1669.

Pancha, A., T. H. Webb, G. E. Stedman, D. P. McLeod, and U. Schreiber (2000), Ring laser detection of rotations from teleseismic waves, *Geophys. Res. Lett.*, **27**, 3553-3556.

Spillman, W. B., D. R. Huston, and J. Wu (1998), Very long gauge length fiber optic seismic event detectors. Proceedings of the SPIE, 3555, 311–321.

Spudich, P., L. K. Stek, M. Hellweg, J. B. Fletcher, and L. M. Baker (1995), Transient stresses at Parkfield, California, produced by the M 7.4 Landers earthquake of June 28, 1992: Observations from the UPSAR dense seismograph array. *Journal of Geophysical Research*, **100**, 675–690.

Spudich, P., J.B. Fletcher (2008), Observation and prediction of dynamic ground strains, tilts and torsions caused by the M6.0 2004 Parkfield, California, earthquake and aftershocks derived from UPSAR array observations, Bull. Seis. Soc. Amer., in print.

Takeo, M. (1998), Ground rotational motions recorded in near-source region of earthquakes. *Geophys. Res. Lett.*, **25**, 789–792.

Teisseyre, R. (2004), Spin and twist motions in a homogeneous elastic continuum and crossband geometry of fracturing. *Acta Geophys Pol*, **52**, 173–183.

Wang, H.J. (2007), Source-dependent variations of M7 earthquakes in the Los Angeles Basin, Doctor thesis, Ludwig-Maximilian-University.

Wang, H.J., H. Igel, F. Gallovic, A. Cochard and M. Ewald (2008), Numerical Green's Functions in 3D medium: Application to the Newport-Inglewood Fault, Los Angeles Basin, in press in Geophys. J. Int.

Yamaguchi, R. and T. Odaka (1974), Field study of the Izu-Hanto-oki earthquake of 1974. Special Bull Earthq Res Inst, Univ Tokyo, **14**, 241–255.

Zembaty, Z. B. (2006), Deriving seismic surface rotations for engineering purposes. Earthquake Source Asymmetry Structural Media and Rotation Effects, Springer Verlag.

Zembaty, Z. and G. Boffi (1994), Effect of rotational seismic ground motion on dynamic response of slender towers. *Europ Earthquake Engng*, **8**, 3–11.

Table 1: Setup for the finite difference modeling in the Los Angeles basin

Spatial discretization (km)	0.3
Time step (s)	0.018
Lowest *S*-wave velocity (km/s)	1.4
Simulation time (s)	65
Number of cells	320×350x100
PML (Perfectly Matched Layer) Nodes	15
Fault area (km^2)	18x36
Top depth (km)	1.5

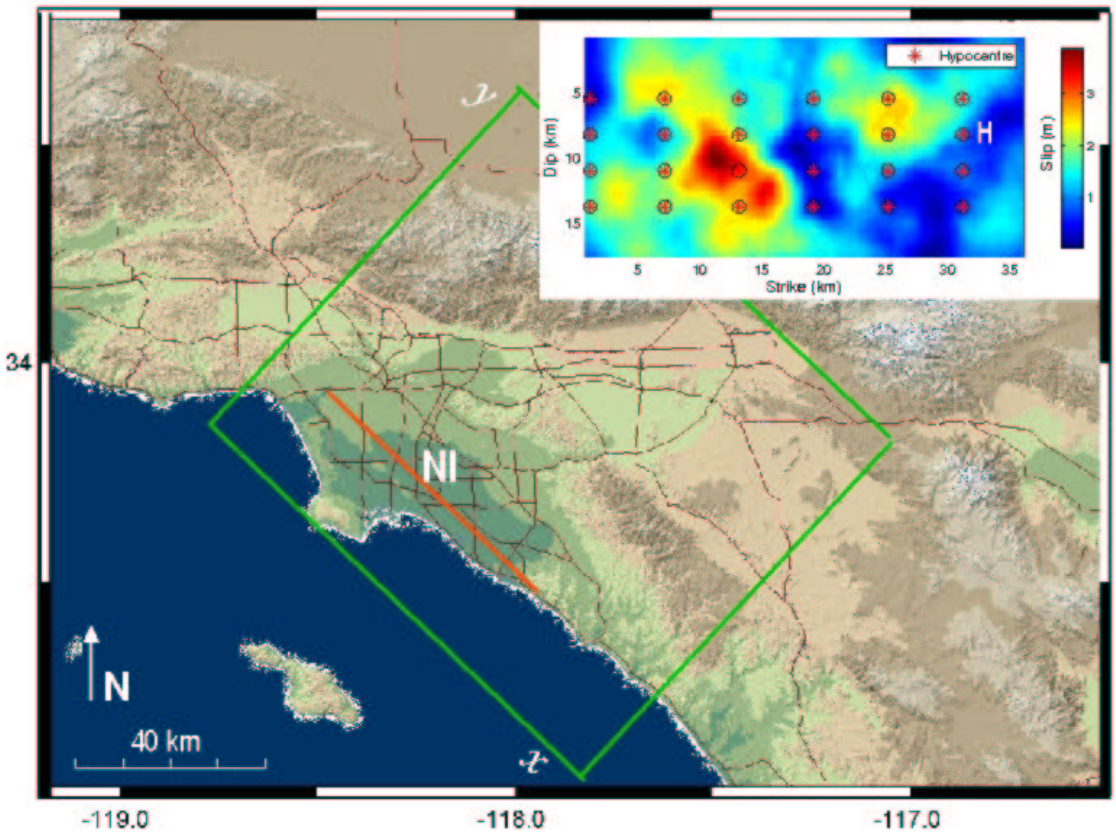

Figure 1: Los Angeles area with modeling region (green rectangle) and the idealized Newport-Inglewood fault (NI, red line). Inlet: An example of final slip distribution of an M7 earthquake on the vertical NI fault plane and hypocenter grid (red asterisks, for investigation of hypocentral effect on ground motion). H is one such hypocenter, as referred later in the text.

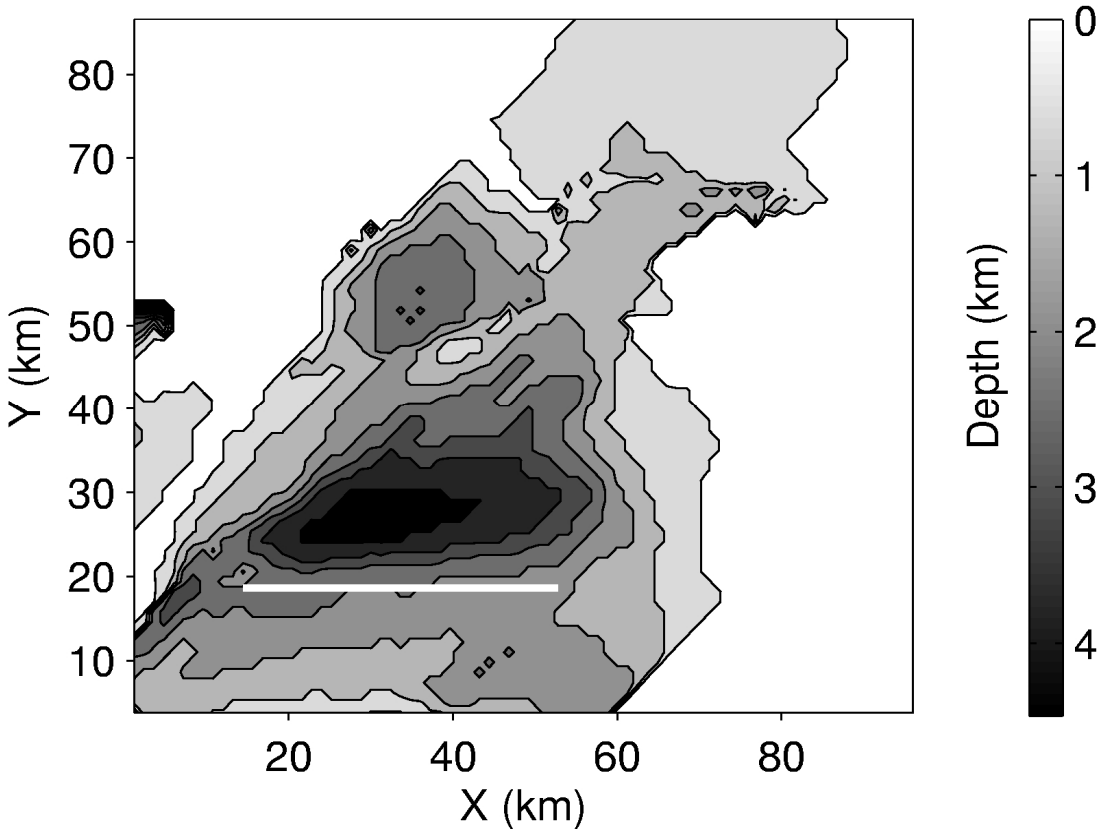

Figure 2: Depth of the 2 km/s shear wave velocity isosurface at (grey scale). The thick white line indicates the fault trace of the M7 scenario earthquake.

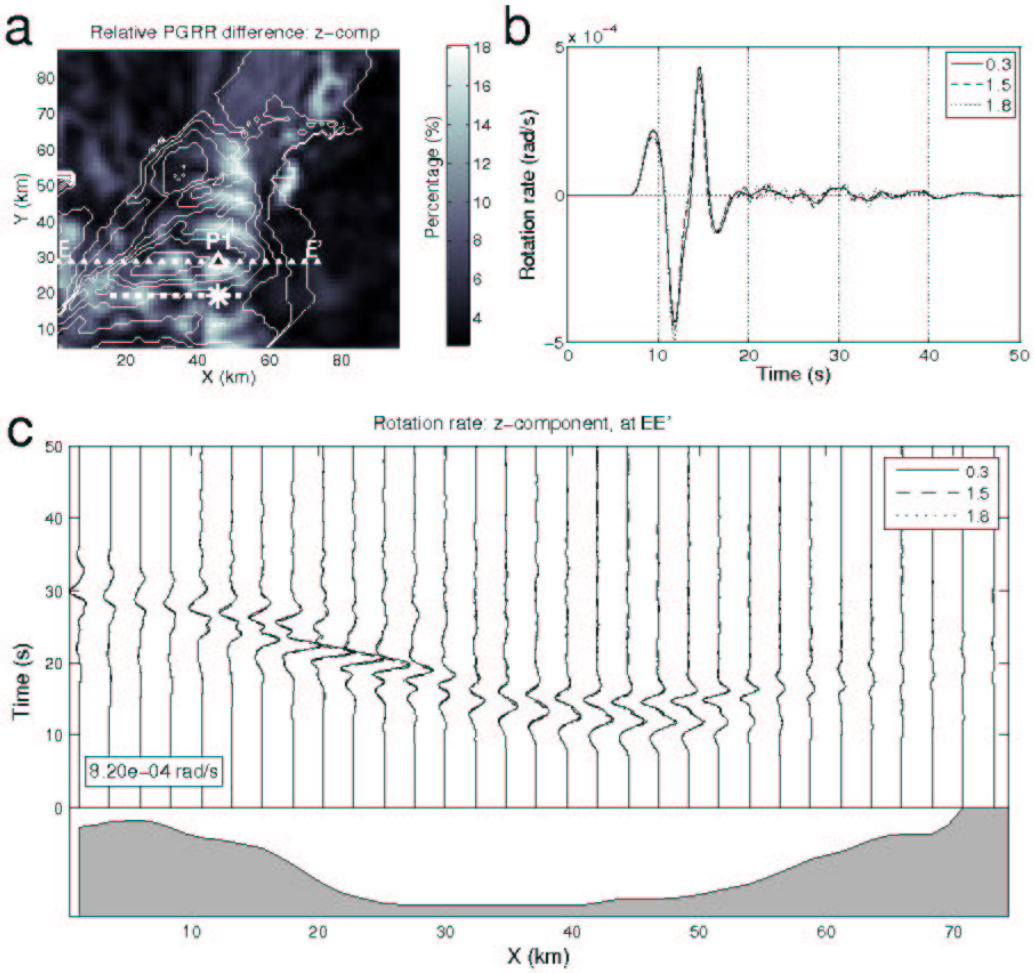

Figure 3: Effect of fault discretization on rotation rate. **a**. Relative peak ground rotation rate (PGRR) difference (z-component) between the solution for the 1.8 km subfault size and the "continuous" solution (subfault size of 0.3 km, corresponding to the finite difference grid step). The dashed thick white line marks the fault trace and the white asterisk shows the epicenter. **b**. Rotation rate seismograms (z-component) from different solutions (subfault sizes of 0.3 km, 1.5 km and 1.8 km) at receiver P1 (largest misfit). **c**. Rotation rate profile along EE' (see panel a) in which the depth of shear wave velocity isosurface at 2.0 km/s is shown at the bottom. The largest rotation rate amplitude across this profile is shown (inlet).

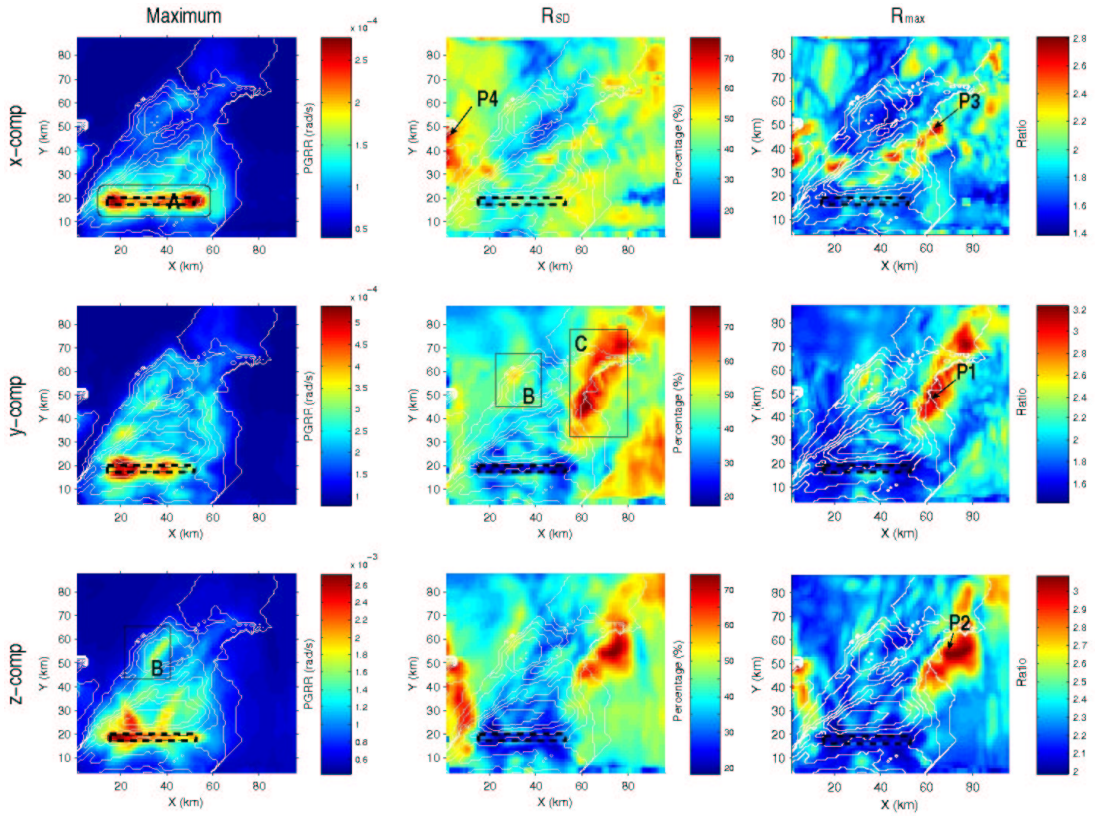

Figure 4: Peak ground rotation rate maps and their variability when using 24 hypocenter positions. **Left**. Maximum value. **Middle**. R_{SD} (ratio between the standard deviation and the mean PGRR value). **Right**. R_{max} (ratio between the maximum value and the mean value). From top to bottom are the x-, y-, and z-components, respectively. The black dashed rectangle is used to indicate the fault trace in order to avoid masking the high values on the fault trace. Thin white lines are contours of the 2 km/s shear velocity isosurface. Regions A, B, and C, and stations P1, P2, P3, and P4, are indicated for discussion in the text. Note the color scale difference among individual plots.

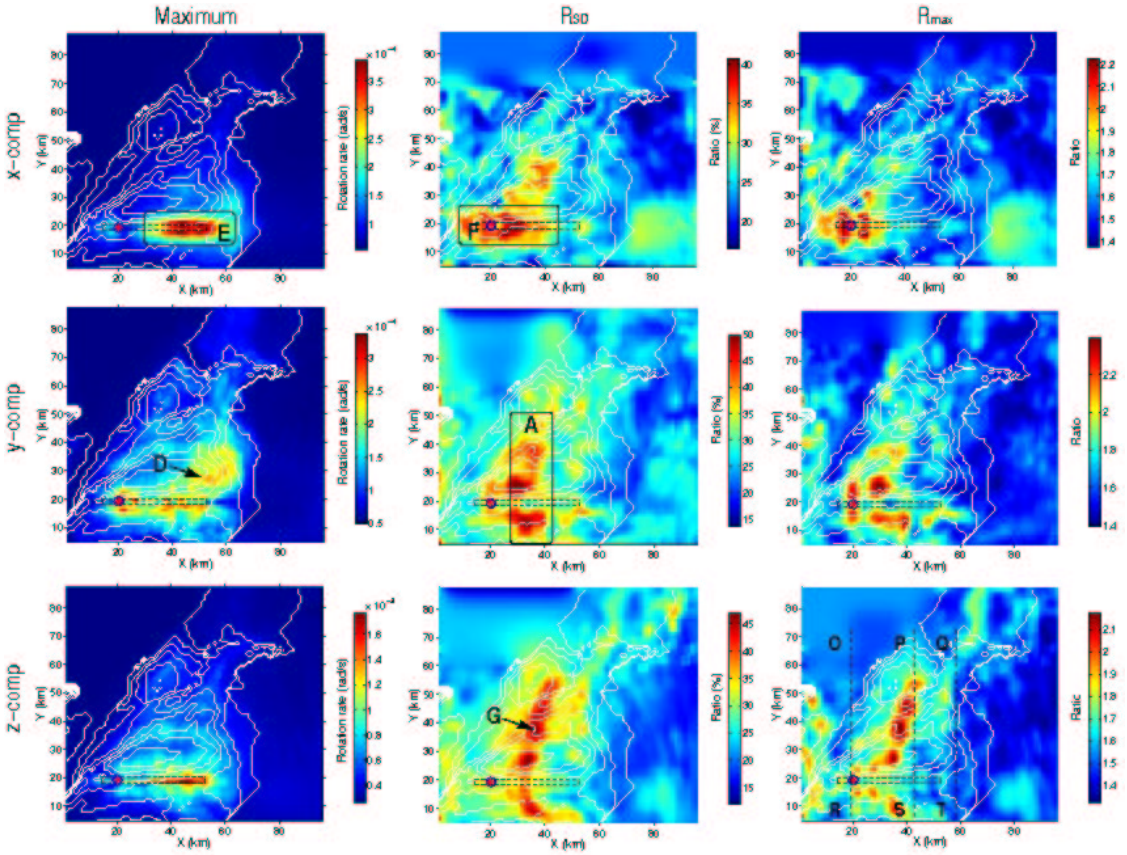

Figure 5: Same as Fig. 4 but for random variations of the slip history with a fixed hypocenter (epicenter indicated by the red dot). Regions A, E and F, stations D and G, and profiles OR, PS and QT are indicated for discussion in the text.

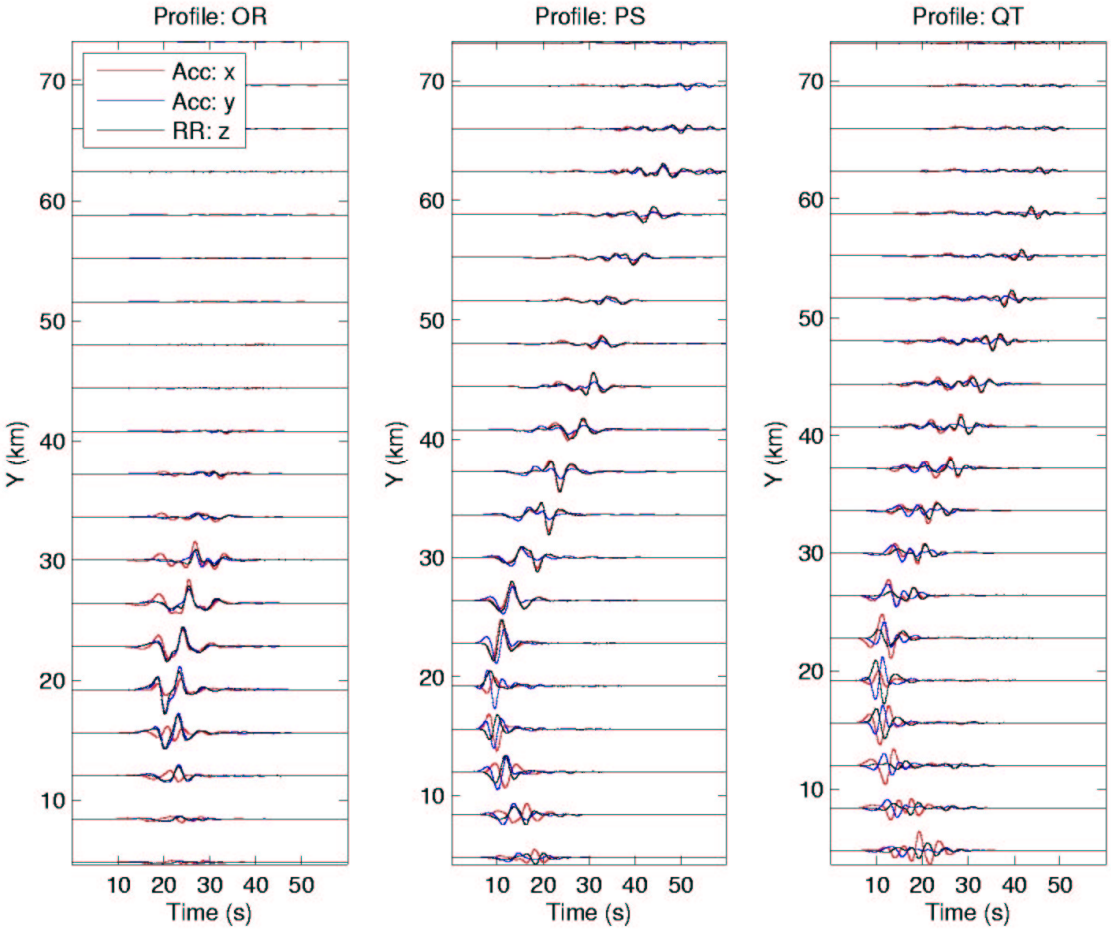

	Profile: OR	Profile: PS	Profile: QT
Acc: x (m/s^2)	2.786	1.449	0.873
Acc: y (m/s^2)	2.821	1.787	1.373
RR: z (1.e-3 rad/s)	2.753	1.747	0.931

Figure 6: Acceleration (horizontal components) and rotation rate (RR, z-component) along the profiles shown in Fig. 5, bottom right. The accelerations and rotation rates are scaled by their maximum amplitude for the corresponding profile (see table above).

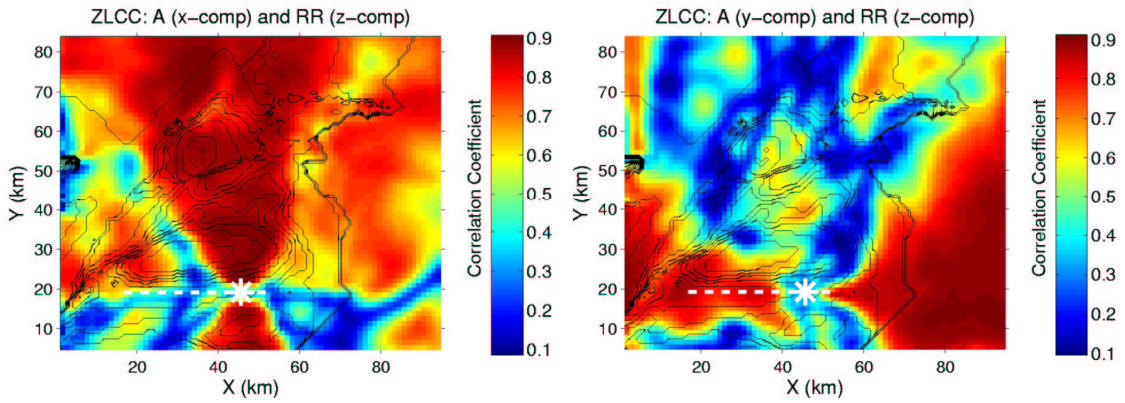

Figure 7: Waveform similarity on the surface between horizontal accelerations and vertical rotation rates for the selected scenario with hypocenter H of inlet of Fig. 1. Zero-lag correlation coefficients (ZLCC) between the waveforms are plotted over the entire study area. **Left**. x-component of acceleration. **Right**. y-component of acceleration. The contours of the 2.0 km/s shear wave velocity isosurface at 2.0 km/s are depicted with the thin black lines. The white thick dashed line marks the fault trace and the white asterisk marks the epicenter.

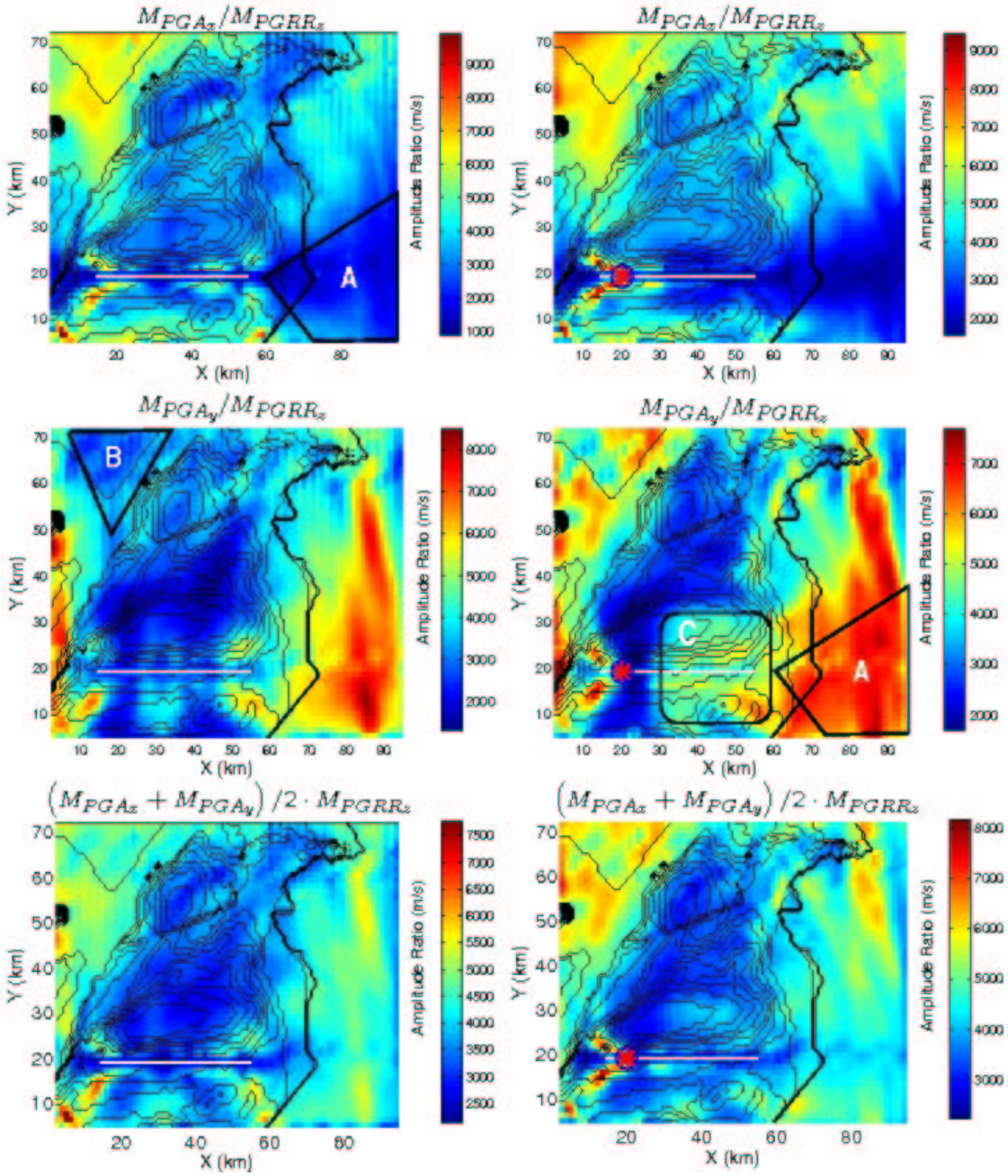

Figure 8: Maps of ratios between peak acceleration and peak rotation rate (z-component). **Left**. Varying hypocenter. **Right**. Varying slip history. **Top**. Acceleration: x-component. **Middle**. Acceleration: y-component. **Bottom**. Geometric mean of the two horizontal accelerations. Black curved lines mark the contours of the 2.0 km/s shear-wave velocity isosurface. The red asterisk marks the epicenter for the case of varying slip history. The white line marks the fault trace. Regions A, B and C are indicated for discussion in the text. Note the color scale difference.

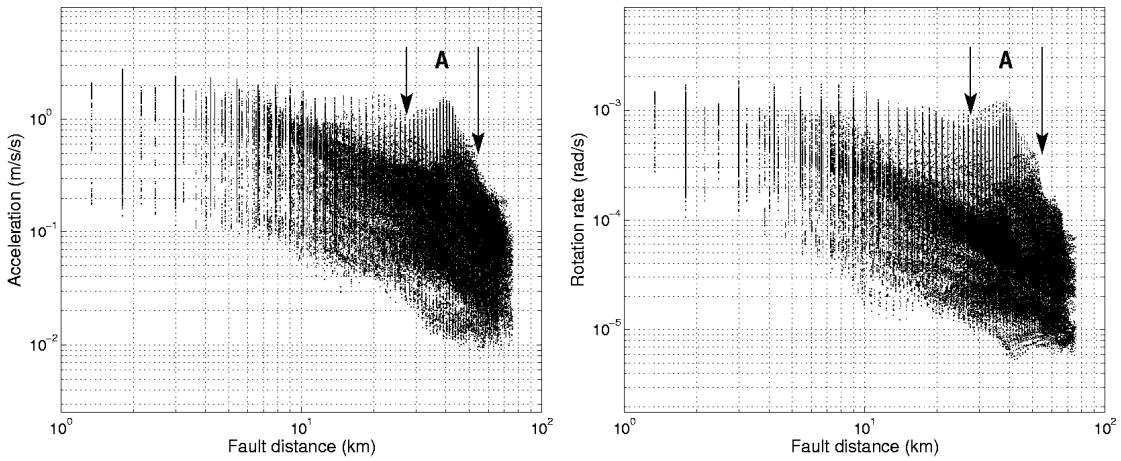

Figure 9: Comparison of peak ground accelerations and peak ground rotation rates as a function of distance to the fault when varying hypocenter location. **Left**. y-component of acceleration. **Right**. z-component of rotation rate. Fault distance range denoted as A is shown for discussion in the text.